

RESEARCH LETTER

Open Access



Source characteristics of the 16 June 2020 M_L 5.4 earthquake and its significant aftershock sequences, northern Red Sea, Egypt

Hamada Saadalla* and Ahmad Hamed

Abstract

The northern Red Sea in eastern Egypt is one of the world's newest marine basins. The northern Red Sea is a very active seismic region and poses a significant hazard to the nearest cities on the Red Sea coast. On June 16, 2020, a moderate earthquake ($M_L = 5.4$), as published by the Egyptian National Seismic Network (ENSN), occurred in the northern Red Sea followed by several aftershocks, ranging in magnitude from 2.0 to 3.4. The best-fitting double-couple movement obtained using the full waveform moment tensor inversion of the main earthquake indicated strike-slip movement, with a minor normal component. The two nodal main shock planes were oriented NNE–SSW and ESE–WNW, respectively. The aftershocks sequences distribution did not coincide with the 16 Jun, 2020 main earthquake, neither in map view nor with respect to depth which may pointed to a secondary fault plane activation and stress triggered by the mainshock. The aftershocks clustered at the north western side of the main earthquakes and extend in the north western direction, which supported that the ESE–WNW plane is the fault plane. The spectral parameters of the S-wave displacement spectra of the main earthquake and its significant aftershock sequences were determined using the spectral inversion method and Brune's ω^2 modulation. The obtained spectra are flat in the frequency range from 0.8 Hz to each corner frequency, and they decreased rapidly at frequencies of < 10 Hz. The calculated seismic moment, moment magnitude, corner frequency, source radius, and stress drop vary from $8.293\text{E}+18$ to $7.541\text{E}+22$ dyn-cm, 2.4 to 5.0, 2.2 to 8.2 Hz, 171 to 633 m, and 0.02 to 13 MPa, respectively. The moment magnitude is equal to or slightly higher than the local magnitude reported by ENSN. The calculated stress drops for the earthquakes increased with increasing earthquake size.

Keywords: Red Sea earthquakes, Full moment tensor inversion, S-wave source spectra

Introduction

The northern Red Sea and the southern portion of the Gulf of Suez are an extensional stress system, whereas the tectonic deformation of the Gulf of Aqaba–Dead Sea fault system is regulated by a shear stress system (Abdel-Fattah et al. 2006). In the northern Red Sea and the Gulf of Suez, geodynamic extension is prominent and results in normal faults, while oblique extension results in sinistral strike-slip and dip-slip faults along the Aqaba–Dead Sea

fault. The majority of earthquakes in the northern Red Sea are low to moderate. On March 31, 1969, an $M_L = 6.8$ earthquake, the maximum recorded to date, was detected in the northern region of the Red Sea, accompanied by many small and moderate earthquakes with magnitudes of < 6.0 (Daggett et al. 1986; Badawy 1999). An earthquake of moderate local magnitude ($M_L = 5.4$) occurred on June 16, 2020 at 14:30 GMT in the northern Red Sea, eastern Egypt. Previous studies and findings about earthquake source characteristics and faulting mechanisms in the northern region of the Red Sea have revealed that in the northern Red Sea and the southern part of the Gulf of Suez, shear stress results in normal movement, with a

*Correspondence: hsaadallah88@nriag.sci.eg

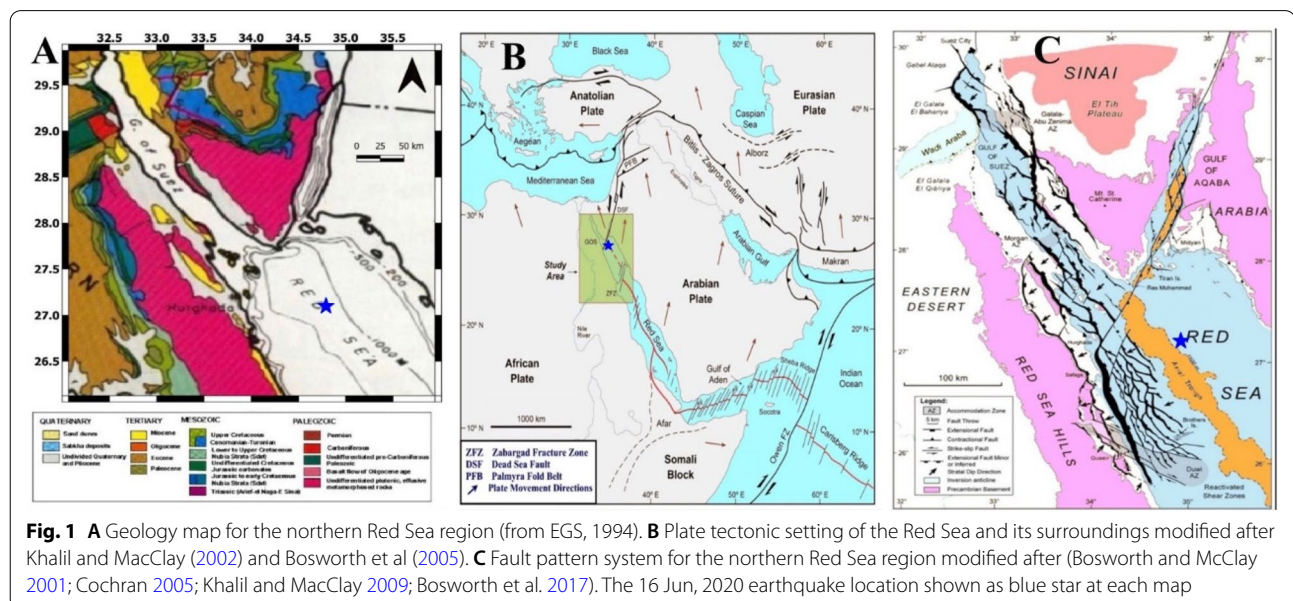
National Research Institute of Astronomy and Geophysics, NRIAG, Helwan, Cairo 11421, Egypt

minor strike-slip component and nodal planes oriented NW–SE, whereas the oblique extension and tectonic deformation of the Gulf of Aqaba–Dead Sea fault system results in strike-slip movement, with minor dip-slip motion and NNE–SSW-oriented nodal planes (e.g., Badawy 1999; Abdel-Fattah et al. 2006; Hussein et al. 2013; Abdel-aal and Yagi 2017; Badreldin et al. 2019; Saadalla et al. 2020). This moderate earthquake was felt in many cities on the western Red Sea coast, including Hurghada city (a highly populated city and a main tourism center). Therefore, a comprehensive study of its mechanism and source features and their spectral parameters is important for future ground motion modulation studies and earthquake hazard analyses. The source movement mechanism, spectral features, and characteristics of the main earthquake and its significant aftershock sequences were estimated. The main earthquake was analyzed using the full waveform moment tensor inversion method (Herrmann 2013), and the movement type of the causative fault was determined. The main earthquake and its significant aftershock sequences were comprehensively investigated using the spectral inversion method, and the spectral parameters were calculated (i.e., seismic moment, moment magnitude, corner frequency, source radius, and stress drop).

Background geology and structure

Three tectonostratigraphic phases are found in the northern Red Sea stratigraphic section (Fig. 1A): pre-rift, syn-rift, and post-rift. The Red Sea is still rifting, so post-rift rocks are only present in the Suez Rift (Said 1990; Khalil and McClay 2001). Gulf of Suez and northern Red

Sea pre-rift rocks comprise platform sedimentary strata unconformably overlying Precambrian crystalline basement rocks (Saleh et al. 2006). The Proterozoic-aged Precambrian basement rocks of the Gulf of Suez and northern Red Sea are visible on the rift flanks and in the eroded-up dip regions of tilted fault blocks inside the rift, including many rift blocks in the vicinity of the northwest coastal Red Sea (Khalil and McClay 2016). These Precambrian basement rocks are unconformably overlain by non-metamorphosed to gently metamorphosed intermediate to silicic volcanics (Dokhan volcanics) and the clastic sedimentary rocks of the Hammamat Group. They are composed of serpentinites, metavolcanics, metasediments, and metagabbros aligned with gneisses in structural highs (El Gaby et al. 1990). Tectonically, both the Gulf of Suez and the Red Sea formed by continental rifting during the early stages of Arabia splitting from Africa. According to several tectonic theories, the rifting spread from the Red Sea into the Suez Rift during the Middle Miocene, eventually becoming an abortive continental rift in the Precambrian shield south of Sinai (Ghebreab 1998; Bosworth et al. 2005). The active Gulf of Aqaba was formed as the Arabian plate split from the Sinai sub-plate, and it has remained active since the Middle Miocene orogeny (Mart and Horowitz 1981; Mart and Rabinowitz 1986). The three areas (Red Sea, Gulf of Suez and Gulf of Aqaba) form a triple junction at the southern extremity of the Sinai Peninsula (Red Sea, Gulf of Suez and Gulf of Aqaba) (Fig. 1B). The rifting process began in the Late Oligocene to Early Miocene and has continued ever since (Bosworth and McClay 2001; Cochran 2005). Four mega-half grabens with exact reverse tilt patterns



have been identified in the Suez Rift and the north western region of the Red Sea. The positions and alignments of the accommodation regions of these mega-half grabens were regulated by pre-rift structures (Fig. 1C). According to several focal mechanism and tectonic investigations, right-lateral shearing forces dominate the northern section of the Gulf of Suez, while approximately NNE–SSW-oriented extensional strain completely dominates the northern Red Sea region (Hempton 1987). The Red Sea is a relatively young and active continental rift system that was initiated in the Late Oligocene–Early Miocene (Coleman 1993; Bosworth et al. 2005). It formed in response to the northeast separation of the Arabian plate from the African plate (Hempton 1987). By the late Middle Miocene, the opening of the Red Sea was linked to sinistral strike-slip displacements along the Gulf of Aqaba–Dead Sea transform fault system. The Suez Rift and the northwest Red Sea rift are characterized by a zig-zag fault pattern, composed of NW–SE and NS to NNE–SSW striking extensional fault systems on the rift borders and within the rift basins (Meshref 1990; Patton et al. 1994; McClay et al. 1998). Other subsidiary fault trends (WNW–ESE and NE–SW) also exist in the Gulf of Suez and the northwest Red Sea.

Seismicity and the dataset

The number of seismic stations in Egypt has increased, and existing stations have been updated with highly sensitive seismic sensors. As a result, earthquakes are being detected more accurately. The majority of earthquakes in the northern Red Sea are of low-to-moderate magnitude. In comparison, multiple moderate- to high-magnitude earthquakes are concentrated along the rift axis in

the southern Red Sea and Afar (Al-Ahmadi et al. 2014). A seismicity map created for the study area includes historical and instrumental seismic events with M_w values of <1 to 7.3 for the period up to 2020. The data were collected from Maamoun (1979), Maamoun et al. (1984), Kebeasy (1990), Ambraseys et al. (1994), Abou Elenean (1997), Badawy (1999), Riad et al. (2004), Badawy et al. (2010), Sawires et al. (2016), and the Egyptian National Seismic Network (ENSN) (Fig. 2A). The distribution of the earthquake epicenters indicates a significant level of activity along the entrance to the Gulf of Suez, and the relative movement of the African and Arabian plates in the Sinai has been ascribed to this activity (Daggett et al. 1986). The most recent maximum earthquake (local magnitude $M_L = 6.8$) was recorded on March 31, 1969. It was situated 80 km NE of Hurghada (Daggett et al. 1986; Badawy 1999). According to Daggett et al. (1986), the adjustment of motion at the triple junction of the Arabian plate, the African plate, and the Sinai sub-plate is what causes the high rate of seismicity in the north-west Red Sea. The data set was composed of the June 16, 2020 main shock and its significant aftershock sequences (Fig. 2B). The selected earthquakes were monitored by the broadband three-component seismic stations of the ENSN. In addition, a few seismic stations from international networks, such as GEOFON (<http://www.iris.edu>) were included to ensure good azimuthal coverage of the main earthquake (Fig. 2B). The data set was relocated using the HYPOINVERSE-ATLAS package (Klein 1978), and the relocated origin parameters are summarized in Table 1. The studied aftershock sequences are mostly of a smaller magnitude $2 \leq M_L \leq 3.4$, while the magnitude of the main earthquake was $M_L = 5.4$. Spectral inversion

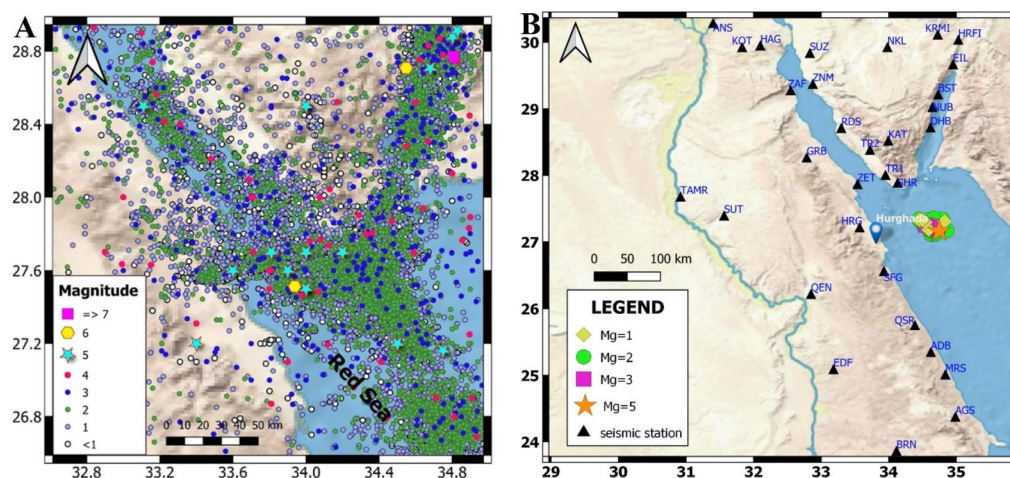


Fig. 2 **A** Seismicity of the northern Red Sea, Gulf of Suez and Gulf of Aqaba based on the compiled earthquake catalogs. **B** The selected dataset and the recorded seismic stations

Table 1 The relocated origin parameters of the 16 Jun, 2020 earthquake and its significant aftershocks sequences

No.	Y	M	Day	H	M	Sec.	Lat.	Long.	Depth	RMS	ERH	ERZ	Mag.
1	2020	6	16	14	30	24.4	27.16	34.75	4	0.31	1.15	2.13	5.5
2	2020	6	16	15	58	2.18	27.25	34.52	21	0.09	1.32	0.55	2.9
3	2020	6	16	16	19	22.92	27.13	34.64	22	0.01	0.86	1.61	2.4
4	2020	6	16	16	40	45.48	27.25	34.45	27	0.33	3.46	1.53	2.0
5	2020	6	16	16	56	51.99	27.27	34.54	22	0.06	1.12	0.49	2.5
6	2020	6	16	17	6	51.88	27.25	34.57	23	0.22	1.48	0.62	3.4
7	2020	6	16	17	44	36.41	27.22	34.56	25	0.39	2.33	1.05	3.1
8	2020	6	16	18	18	33.09	27.21	34.61	22	0.27	1.56	1.11	2.2
9	2020	6	16	19	35	1.56	27.26	34.57	22	0.16	1.47	0.56	3.1
10	2020	6	16	23	11	21.53	27.20	34.63	16	0.13	0.78	0.55	3.3
11	2020	6	17	16	43	3.55	27.22	34.61	21	0.28	1.44	0.78	3.2
12	2020	6	17	18	12	35.44	27.24	34.60	19	0.18	1.3	0.6	2.9
13	2020	6	17	21	38	53	27.29	34.57	22	0.21	1.34	2.29	2.7
14	2020	6	17	23	1	50.97	27.23	34.63	17	0.14	1.02	0.6	2.6
15	2020	6	18	0	37	36.7	27.31	34.53	14	0.08	1.17	0.76	2.4
16	2020	6	20	19	47	28.41	27.25	34.58	22	0.28	1.57	0.86	2.9
17	2020	6	21	21	37	17.75	27.30	34.56	10	0.13	1.3	1.09	2.4
18	2020	6	22	8	33	0.88	27.28	34.56	12	0.14	1.1	2.14	2.9
19	2020	7	5	18	41	7	27.31	34.47	22	0.11	1.35	0.98	2.4
20	2020	7	13	10	13	30.8	27.25	34.52	23	0.12	1.18	0.57	2.8
21	2020	7	15	20	26	23.18	27.34	34.76	16	0.1	2.81	0.65	2.6
22	2020	8	3	5	30	33.56	27.61	34.37	28	0.17	1.99	0.71	2.6
23	2020	8	9	23	23	6.76	27.62	34.50	21	0.1	1.23	0.66	2.9
24	2020	8	13	22	59	48.31	27.72	34.38	21	0.26	0.81	0.71	3.3
25	2020	8	16	1	42	30.6	27.30	34.46	19	0.1	1.45	0.56	2.5
26	2020	8	16	12	27	48.83	27.61	34.33	13	0.09	1.14	1.03	2.2
27	2020	8	19	12	17	8.33	27.30	34.53	9	0.13	1.14	1.88	2.2
28	2020	8	19	20	26	18.63	27.62	34.18	7	0.09	0.87	0.98	2.6
29	2020	8	22	2	4	10.58	27.46	34.47	24	0.27	2.53	0.85	3.0
30	2020	8	23	16	27	58.77	27.47	34.24	29	0.08	1.73	0.53	1.9

H: hour; M: minute; Sec.: second; Lat.: latitude; Long.: longitude; RMS: root mean square; ERH: horizontal error; ERZ: vertical error; Mag.: local magnitude

was applied to the main earthquake and its significant aftershock sequences, while full moment tensor inversion was only performed for the main shock. Table 1 lists the origin parameters of the studied events.

Methods

Moment tensor analysis

Applying moment tensor analysis using full waveform required some specific preparation of the recorded earthquake data. The waveform data were stored in SEED format, with a sampling frequency 100 Hz. The waveform data were processed as follows. First, the original recordings of the main earthquake were prepared by identifying and removing the mean and linear trends, the waveform was resampled, and traces were

tapered and corrected by removing the instrument response (Fig. 3A). The displacement seismograms were then rotated and filtered (Fig. 3B). Only earthquakes with a good signal-to-noise ratio were used for the analysis (Fig. 3C). Second, the wavenumber integration (Herrmann and Wang 1985) method was used to compute the synthetic Green's functions for the northern Red Sea using Hosny et al.'s (2009) velocity model (Table 2). The calculated elastodynamic Green's functions and the observed seismograms were filtered by the same frequency band in the range of 0.02 to 0.06 Hz to suppress and remove bad signals from the data. This frequency band range is reasonable for moderate earthquakes, as recommended by Havskov and Ottemoller (2010) and Zhang et al. (2016). Finally, full inversion of

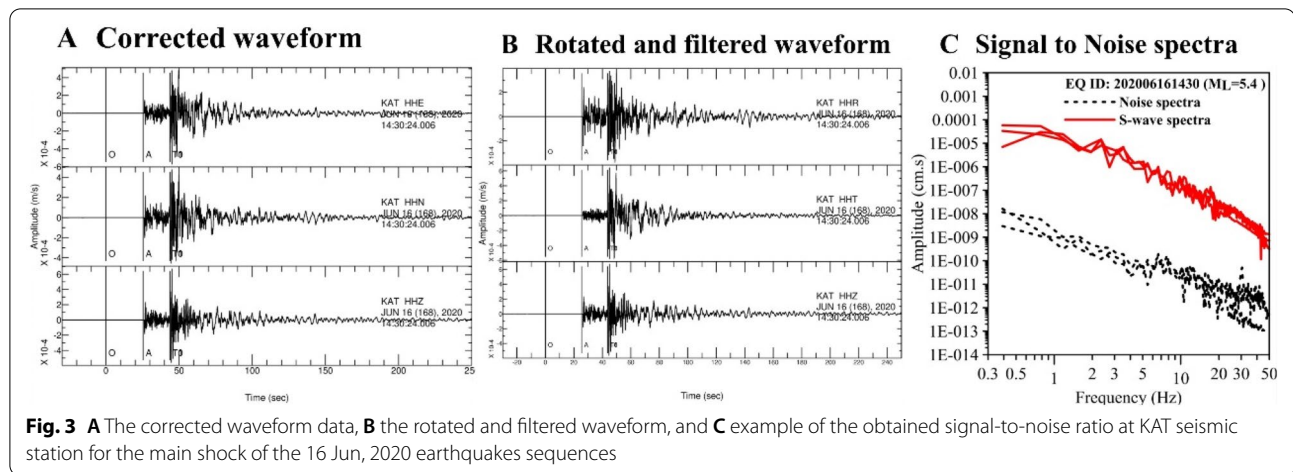


Table 2 Velocity model for the northern Red Sea after Hosny et al. (2009) utilized for calculation of the synthetic seismograms and spectral parameters

Depth (km)	Vp (km/s)	Vs (km/s)	Density (kg/cm ³)	Qp	Qs
0.0	4.3	2.5	2.5	225	100
1.0	4.5	2.6	2.5	225	100
3.0	5.9	3.4	2.8	225	100
9.0	6.3	3.6	2.9	325	100
12.0	6.5	3.8	2.9	226	100
20.0	6.8	4.0	3.0	225	100
25.0	7.5	4.4	3.2	225	100
32.0	8.1	4.7	3.3	1000	450
40.0	8.2	4.8	3.4	1000	450

the moment tensor was applied to selected traces based on an algorithm in a seismology computer program written by Herrmann (2013). The best double-couple mechanism was performed assuming a point seismic source, a displacement trace d in direction n at an arbitrary position x , and time t , equated as follows (Stump and Johnson 1977):

$$d_n = M_{ij} [G_j * s(t)], \quad (1)$$

where M_{ij} is the moment tensor, the synthetic seismograms are represented by G_j in j direction, $s(t)$ is the source time function, and the time convolution is indicated by the asterisk assuming a delta function of $s(t)$ and a synchronized seismic source. Displacement d_n is a linear function of the elements of the moment tensor, and the computed Green's function leads to linear inversion in the frequency domain, as expressed in Eq. (2),

$$d_n(f, x) = M_{kj}(f) G_{nk,j}(f). \quad (2)$$

The inversion is solved as a least-square problem (Jost and Herrmann 1989), as formulated in Eq. (3):

$$d = Gm, \quad (3)$$

where G is a matrix containing the synthetic seismograms and m is a vector with the six components of the moment tensor. The best-fitting depth, moment magnitude, scalar seismic moment, and fault movement mechanism were selected based on the fitting goodness between the calculated and observed waveforms.

Spectral analysis

The spectral parameters were estimated for the earthquakes by modeling the spectra of the three-component waveform recordings with clear phase arrivals. As a consequence, the waveforms were selected from time windows with a length of 2.56 s starting 0.5 s before the manually picked S-phase arrivals. The 2.56-s window length was selected to avoid contamination with other phases on the seismograms. The spectra were then calculated using a fast Fourier transform (FFT), which was smoothed using a Hanning window length of 5.0 Hz, averaged over the total number of the used station for each event to obtain the average displacement spectra. The corrected source spectra were typically extracted from the observed seismogram after removing the attenuation and site effects using Andrews's (1986) inversion technique, extended by Iwata and Irikura (1988). The inversion technique was performed based on the assumption that the reference station had the

smallest site effect and had an amplification factor of around 2.0 for the whole frequency range, considering the free surface effect. See Saadalla et al. (2019, 2020) for a further description of the inversion technique. First, three seismic stations (i.e., Kathreen [KAT], HRG, and BST), which showed relatively stable horizontal-to-vertical ratio (H/V) curves, were tested. Namely, the spectral inversion was carried out three times using one of the three stations as an alternative reference site, with its H/V curves as the site effect for the reference site. Figure 4A shows an outside view of the KAT seismic station and its surface geology, while Fig. 4B shows the preliminary result of the H/V horizontal-to-vertical spectral ratio at the KAT station using the earthquake's coda-wave. The KAT station was found to have the most reasonable site amplification effect, so it was used as a reference site. The obtained spectra from all available recordings for each event were modeled individually based on the displacement spectrum model for S-waves (Brune 1970) as follows:

$$M_0 = \frac{4\pi\rho v^3}{F \times R_{\theta\varphi} \times G(r, h)} \Omega_0, \quad (4)$$

where ρ is the density, v is the seismic wave velocity, F is the effect of the free surface, $R_{\theta\varphi}$ is the radiation pattern, and $G(r, h)$ is the geometrical spreading effect. The velocity model, after Hosny et al. (2009) was used to calculate the S-wave travel time. For a radiation pattern correction, we used 0.63 for the S-wave (Aki and Richards 2002). The corner frequency was calculated for each source spectra using Andrews's (1986) automated method. Under the assumption of a circular plane fault and a double-couple source, scalar seismic moment M_0 , source dimension r , and stress drop $\Delta\sigma$ can be determined from Ω_0 and f_c using the following relationships (Eshelby 1957; Brune 1970):

$$r = \frac{2.34\beta}{2\pi f_c}, \quad (5)$$

$$\Delta\sigma = \frac{7}{16} \left(\frac{M_0}{r^3} \right). \quad (6)$$

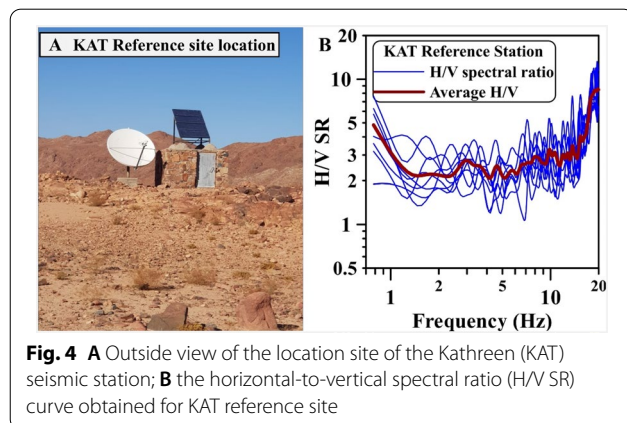
Results

Moment tensor results

Full moment analysis and the best-fitting double-couple mechanism for the June 16, 2020 Red Sea main shock revealed that strike-slip movement with minor normal components dominated, with NNE–SSW and ESE–WNW trending fault planes. The obtained parameters associated with the best-fitting, such as moment magnitude, seismic moment, source depth, best double-couple solution, and fitting variance, are summarized in Fig. 5A. The relocated parameters especially the source depth of the mainshock are consistent with the optimum fitting source depth obtained in this study (Fig. 5B). The aftershocks selected in this study revealed that the plane oriented NNE–SSW toward the Gulf of Suez is the fault plane (Fig. 5C). The mainshock and the aftershocks are relocated, the average root mean square (RMS), the average horizontal error (ERH), the average vertical error (ERZ) are 0.17 s, 1.47 km, 0.98 km, respectively (Table 1). The main shock is located at 4 km depth, where the aftershocks are located at depth range from 8.8 to 28.6 km toward the north western side of the 16 Jun, 2020 main event. In general, the aftershocks sequences distribution did not coincide with the 16 Jun, 2020 main earthquake, neither in map view nor with respect to depth. The fault plane solution of the 16 Jun, 2020 main earthquake is compared with previous finding and solutions (e.g., Saadalla et al. 2020; Badreldin et al. 2019; Mohamed et al. 2015; Hussein et al. 2013; Megahed 2004; Abou Elenean 1997) as shown in Fig. 5D. Figure 6A, B shows examples of the waveform correlation and the location error of the inverted earthquake. To summarize, the correlation between the observed and calculated seismograms was 95% fitting goodness, with a time shift equal to 1.4 s, and data with high signal-to-noise ratios indicated that our results are accurate and robust.

Spectral and source parameter results

All the obtained spectra were flat in the frequency range from 0.8 Hz to each corner frequency and decreased rapidly at frequencies of <10 Hz. The smoothed displacement spectra at each station of each event (Fig. 7A) were inverted, and their average source spectra and standard deviation were calculated (Fig. 7B). Figure 8 shows



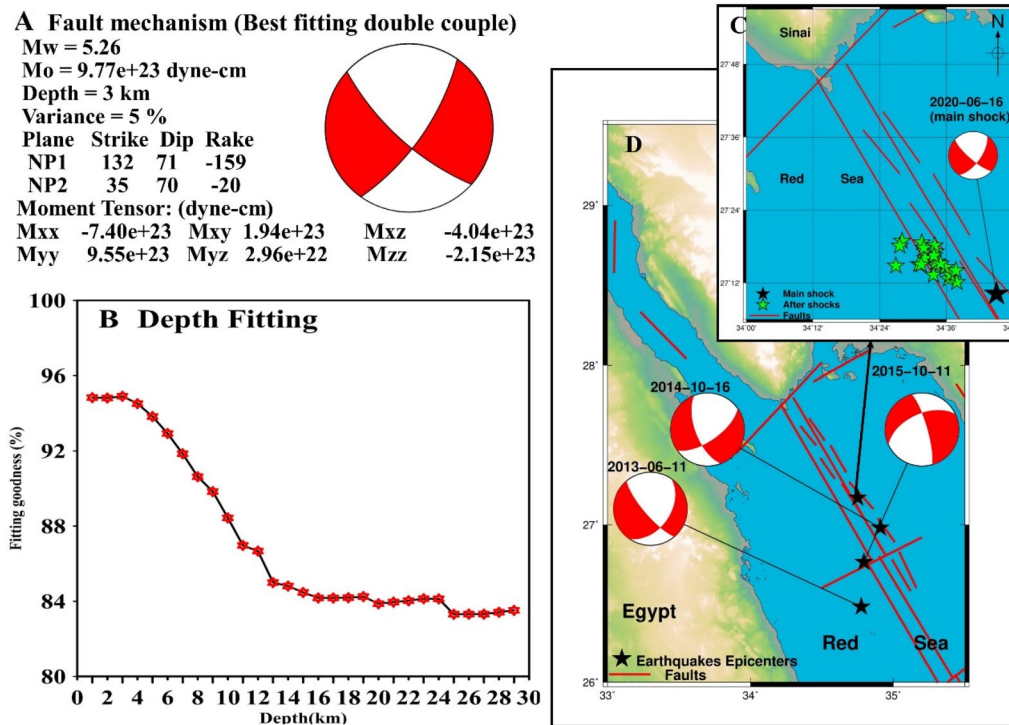


Fig. 5 **A** The best-fitting fault mechanism of the 16 Jun, 2020 earthquake. **B** The correspondence best depth fitting, and **C** the aftershock clustered and distribution with the best double-couple solution of the mainshock; **D** the focal mechanism distribution obtained by previous studies

an example of the good fitting between Brune's (1970) theoretical omega-square model and the observed displacement source spectra of the main earthquake with a moment magnitude of 5.0 and one of the aftershock earthquakes with a moment magnitude 3.0. Based on Brune's (1970) modulation and Andrews's (1986) automation analysis, the seismic moment and corner frequency, respectively, were determined for the studied events. The estimated seismic moment and corner frequency of the main earthquake and its aftershock sequences varied from 8.293×10^{18} to 7.541×10^{22} dyn-cm and 2.2 to 8.2 Hz, respectively (Table 3). Determining the seismic moment and the corner frequency enabled us to estimate the dynamic source parameters for the studied earthquakes, including the moment magnitude, source radius, and stress drop. Table 3 lists the source parameter results for the main earthquake and its significant aftershock sequences. Our results revealed that the estimated value for the moment magnitude M_w , source radius r (m), and stress drop $\Delta\sigma$ (MPa) ranged from 2.4 to 5.0, 171 to 633 m, and 0.02 to 13 MPa, respectively.

The assigned local magnitude catalog derived from the ENSN shows a linear relationship with the determined moment magnitude M_w and the logarithm seismic moment M_0 of the earthquakes investigated in this study (Fig. 9A, B). The determined corner frequencies decayed with increasing seismic moment, while the estimated source radius increased with increasing seismic moment (Fig. 10A, B). The investigated earthquakes were tectonic interplate earthquakes. The stress drop value obtained for the main shock earthquake ($M_L = 5.4$) is 13 MPa, which is much higher than the stress drop values obtained for the aftershock sequences ($M_L \leq 3.3$). The determined stress drop values plotted against the logarithm seismic moment (Fig. 10C) indicate that the stress drop values increase with the increasing seismic moment of the current earthquakes' sequences. The dependence of the obtained source parameters on earthquake depth was also investigated, and our results reveal that the obtained corner frequencies, seismic moments, and stress drops of the main aftershocks of the June 16, 2020 earthquake may be depth dependence (Fig. 11A–C).

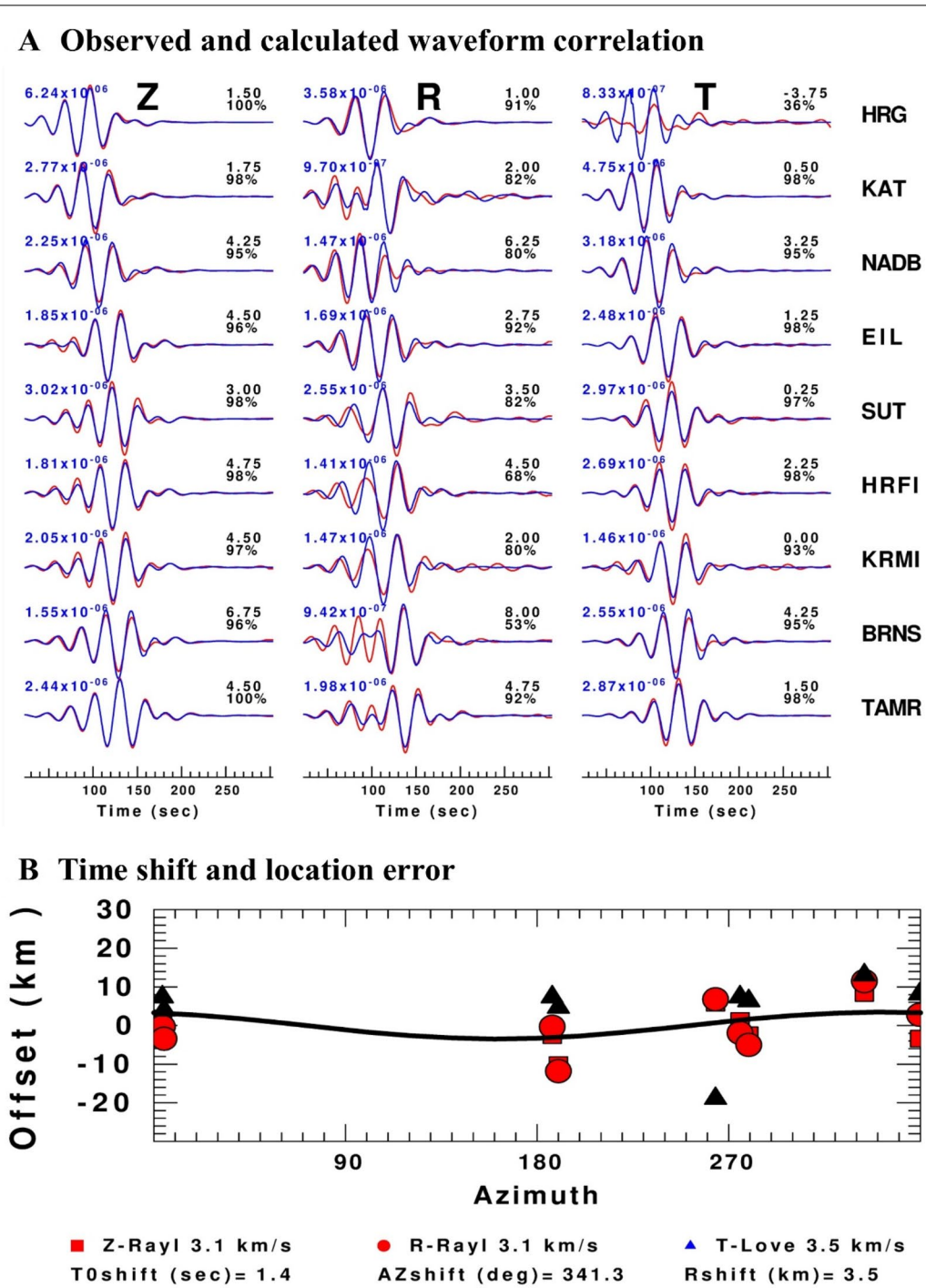


Fig. 6 **A** Synthetic and observed seismograms correlation of the current main shock of 16 Jun, 2020 northern Red Sea. **B** The time shift and location error of the inverted event

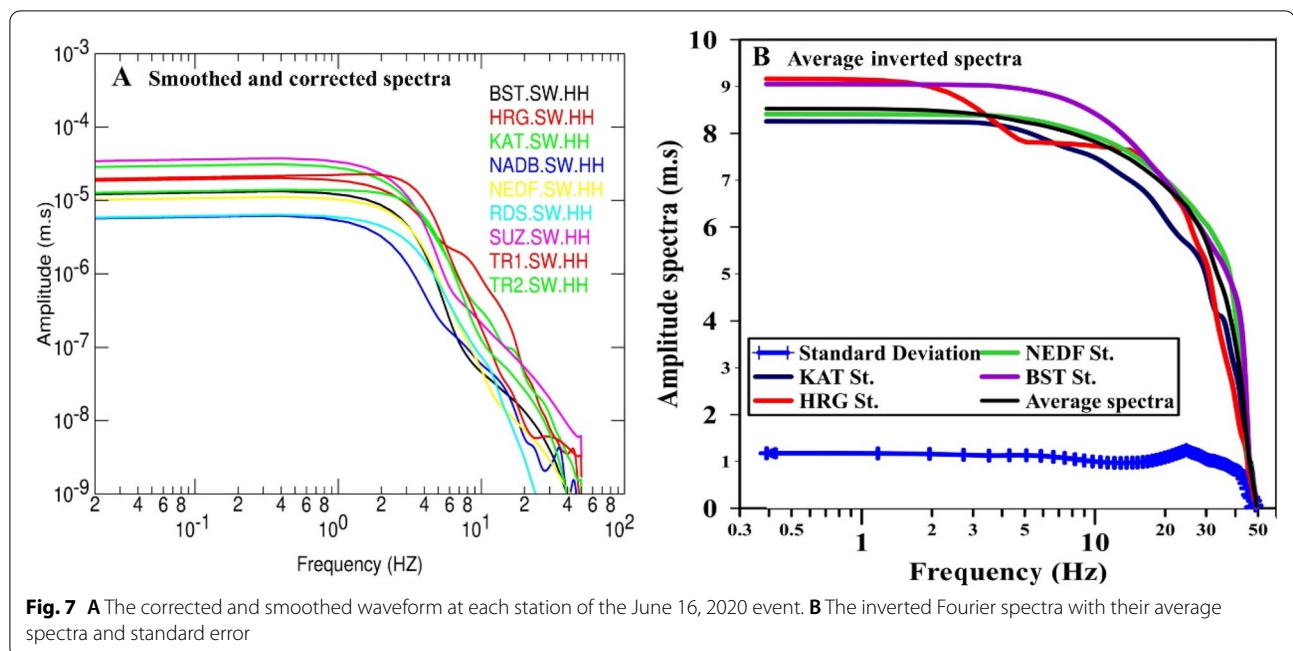


Fig. 7 **A** The corrected and smoothed waveform at each station of the June 16, 2020 event. **B** The inverted Fourier spectra with their average spectra and standard error

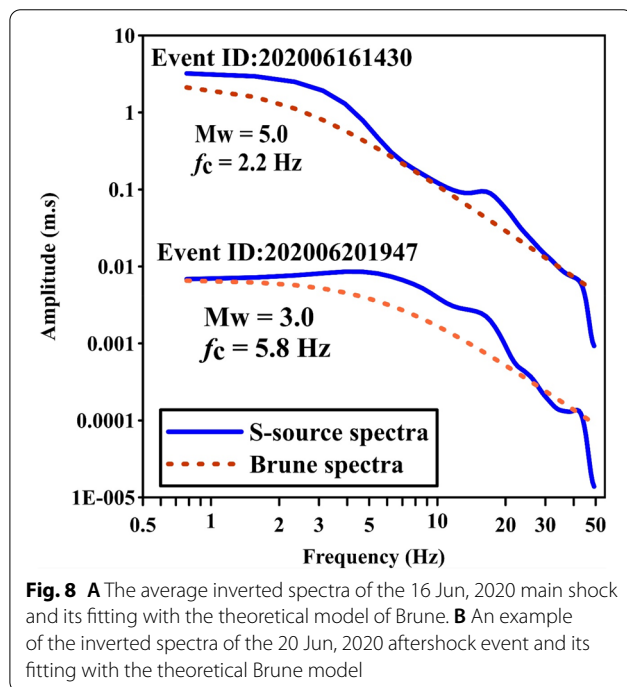


Fig. 8 **A** The average inverted spectra of the 16 Jun, 2020 main shock and its fitting with the theoretical model of Brune. **B** An example of the inverted spectra of the 20 Jun, 2020 aftershock event and its fitting with the theoretical Brune model

Discussion and conclusion

Generally, the northern Red Sea covers a broad area of active tectonics and is characterized by zigzag fault patterns, composed of NW–SE and N–S to NNE–SSW

striking extensional fault systems (Meshref 1990; Patton et al. 1994; McClay et al. 1998). Extensional strain, oriented approximately NNE–SSW, completely dominates the northern Red Sea region (Hempton 1987). The majority of the earthquakes in the northern Red Sea are of low-to-moderate magnitude (Badawy 1999). A moderate earthquake ($M_L = 5.4$) occurred on June 16, 2020, about 80 km NE of Hurgada city in the northern part of the Red Sea. Several aftershocks followed the main event in the same area from June 16, 2020 to August 23, 2020, with magnitudes of < 3.5 . The main earthquake was found to have strike-slip faulting, with minor dip-slip motion and nodal NNE–SSW and ESE–WNW oriented planes. The obtained fault plan solution revealed that the T -axis and P -axis were directed ENE–WSW, which is consistent with the general tension movement along the Red Sea. The aftershocks sequences distribution did not coincide with the 16 Jun, 2020 main earthquake, neither in map view nor with respect to depth. The studied aftershocks are extended and clustered at the north western side of the main shock which may indicated a secondary fault plane activation, or suggested that the seismicity in the north western side were activated by the 16 Jun, 2020 mainshock due to stress triggering (Donner et al. 2013). The best double-couple mechanism determined using the full waveform moment tensor analysis for the current earthquake was consistent with previous findings (e.g., Abou Elenean 1997; Megahed 2004; Hussein et al. 2013;

Table 3 The calculated spectral parameters of the 16 Jun, 2020 earthquake and its significant aftershocks sequences

No.	Ω_0 (dyne-cm)	f_c (Hz)	M_0 (dyne-cm)	$\log M_0$	M_W	M_L	r_0 (m)	$\Delta\sigma$ (MPa)
1	2.38E+00	2.2	7.54E+22	22.9	5.0	5.4	633.1	13.00
2	1.01E-03	6.2	3.21E+19	19.5	2.8	2.9	226.2	0.12
3	4.99E-04	5.9	1.58E+19	19.2	2.6	2.4	237.6	0.05
4	7.07E-04	6.4	2.24E+19	19.4	2.7	2.5	218.8	0.09
5	2.43E-03	7.4	7.71E+19	19.9	3.0	2.5	191.2	0.48
6	3.82E-03	4.7	1.21E+20	20.1	3.2	2.6	301.0	0.19
7	2.26E-03	7.4	7.16E+19	19.9	3.0	3.1	190.3	0.45
8	3.12E-04	6.2	9.89E+18	19.0	2.4	2.2	225.4	0.04
9	1.02E-02	6.5	3.23E+20	20.5	3.4	3.1	217.7	1.37
10	5.12E-03	5.6	1.62E+20	20.2	3.2	3.3	251.8	0.44
11	9.57E-03	4.5	3.04E+20	20.5	3.4	3.2	312.7	0.43
12	1.50E-03	6.2	4.76E+19	19.7	2.9	2.9	226.4	0.18
13	4.32E-04	6.1	1.37E+19	19.1	2.5	2.7	230.6	0.05
14	6.96E-04	5.1	2.21E+19	19.3	2.7	2.6	275.4	0.05
15	5.55E-04	6.2	1.76E+19	19.2	2.6	2.4	226.4	0.07
16	6.66E-03	5.8	2.11E+20	20.3	3.3	2.9	242.6	0.65
17	2.61E-04	7.0	8.29E+18	18.9	2.4	2.4	200.2	0.05
18	6.83E-04	5.1	2.17E+19	19.3	2.7	2.9	275.4	0.05
19	6.18E-04	6.6	1.96E+19	19.3	2.6	2.4	213.1	0.09
20	3.84E-03	5.3	1.22E+20	20.1	3.2	2.8	263.9	0.29
21	6.86E-04	5.1	2.18E+19	19.3	2.7	2.6	275.0	0.05
22	7.72E-04	8.2	2.45E+19	19.4	2.7	2.6	170.8	0.22
23	1.74E-03	3.9	5.52E+19	19.7	2.9	2.9	365.1	0.05
24	2.49E-02	7.1	7.91E+20	20.9	3.7	3.3	197.0	4.53
25	3.85E-04	4.7	1.22E+19	19.1	2.5	2.5	298.7	0.02
26	3.07E-04	7.2	9.75E+18	19.0	2.4	2.2	196.0	0.06
27	1.23E-03	5.7	3.89E+19	19.6	2.8	2.2	246.1	0.11
28	1.33E-03	6.7	4.23E+19	19.6	2.9	2.6	211.2	0.20
29	3.39E-03	5.6	1.07E+20	20.0	3.1	3.0	249.7	0.30
30	6.42E-04	6.0	2.04E+19	19.3	2.6	2.7	235.9	0.07

Ω_0 : relative seismic moment; f_c : S-wave corner frequency; M_0 : absolute seismic moment; M_W : moment magnitude; M_L : local magnitude; r_0 : source radius; $\Delta\sigma$: stress drop

Mohamed et al. 2015; Badreldin et al. 2019; Saadalla et al. 2020). The main objective of the current work was to comprehensively study recent seismicity and its spectral parameters in addition to understanding the tectonic setting of the northern Red Sea and the interaction of its extensional movement with the Gulf of Aqaba and Gulf of Suez for seismic hazard assessment and risk management modulation.

The focal depth of the June 16, 2020 earthquake was very shallow (3 km) compared to the 4 km obtained by the relocation analysis. The investigated earthquakes, including the main earthquake and its significant aftershock sequences, were processed using the generalized

inversion technique constrained by a reference rock site. The corrected displacement source spectra obtained for the earthquakes' sequences were modulated based on Brune's (1970) theoretical model, and the advanced spectral parameters (i.e., seismic moment, moment magnitude, corner frequency, source radius, and stress drop) were extracted. The isolated source spectra modulated very well with Brune's spectra. Based on the shear-wave spectral inversion and Brune's modulation, the spectral parameters using the isolated S-wave displacement spectra were determined. The calculated range of the seismic moment and the corner frequency were reasonable for the magnitude size of the current earthquake sequences.

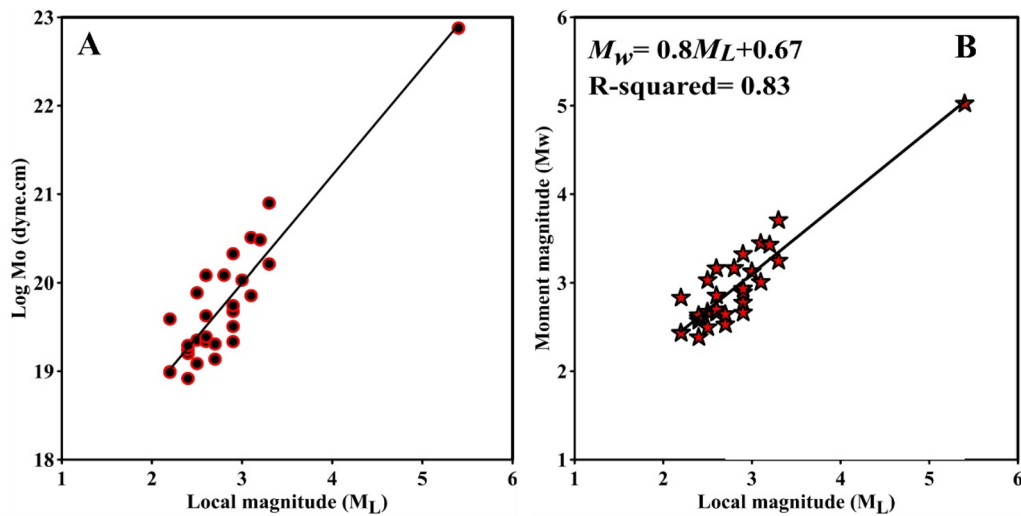


Fig. 9 Regression analysis between the local magnitude assigned by the ENSN and the logarithm of the seismic moment (A) and their linear relation with the moment magnitude obtained for the current events (B)

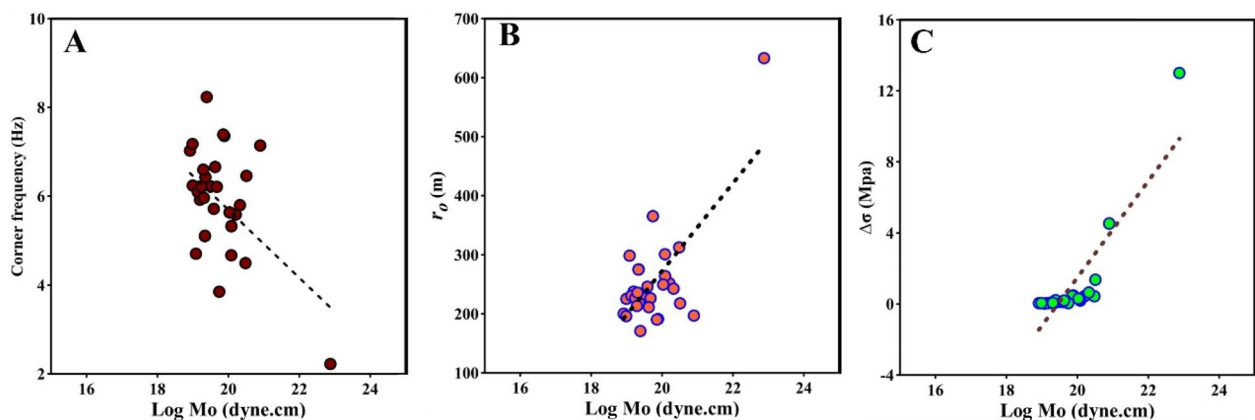


Fig. 10 The dependence of the seismic moment in logarithmic scale on the essential spectral parameters including (corner frequency, source radius, and stress drop)

The estimated moment magnitude was slightly higher than the assigned local magnitude reported by ENSN. Source radius and stress drop values estimated in this study have a linear relationship with the magnitude of the current earthquakes. The calculated stress drop values are in good agreement with the stress drop range of small-to-moderate interplate earthquakes, from 0.1 to

100 MPa (Kanamori 1994), and have depth dependence (the stress drop relatively increased with increasing the earthquakes source depth). As a result, comprehension of the northern Red Sea's tectonic context and the connection of its extensional movement with the Gulf of Aqaba and Gulf of Suez might aid in the evaluation of seismic hazards and the improvement of risk management.

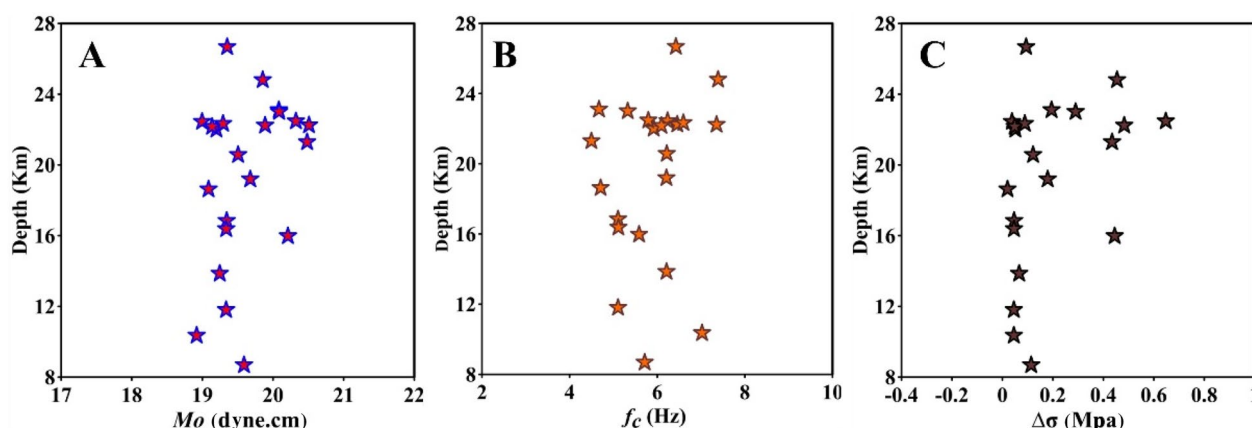


Fig. 11 The dependence of the spectral parameters such as: seismic moment (A), corner frequency (B), and stress drop (C) on the earthquakes depth included in this study

Acknowledgements

We are grateful to the National Research Institute of Astronomy and Geophysics Aswan region earthquake research center and all the staff members of the Egyptian National Seismograph Network for their help and support. We are also grateful to the anonymous reviewers for their valuable comments and recommendations.

Author contributions

HS processed the earthquakes data. The full moment tensor analysis performed by HS, and AH. The authors are involved in the interpretations and integration of the results. Both authors read and approved the final manuscript.

Funding

Not applicable.

Availability of data and materials

The data that support the findings of this study are available from NRIAG but restrictions apply to the availability of these data, which were used under license for the current study, and so are not publicly available. Data are, however, available from the authors upon reasonable request and with permission of NRIAG.

Declarations

Ethics approval and consent to participate

Not applicable.

Consent for publication

Not applicable.

Competing interests

The authors declare that they have no competing interests.

Received: 29 July 2022 Accepted: 9 October 2022

Published online: 25 October 2022

References

- Abd el-aal AK, Yagi Y (2017) Earthquake source characterization, moment tensor solutions, and stress field of small–moderate earthquakes occurred in the Northern Red Sea Triple Junction. *J Geosci* 21:235–251. <https://doi.org/10.1007/s12303-016-0025>
- Abdel-Fattah AK, Hussein HM, El-Hady S (2006) Another look at the 1993 and 1995 Gulf of Aqaba earthquakes from the analysis of teleseismic waveforms. *Acta Geophys* 54:260–279
- Aki K, Richards PG (2002) Quantitative seismology, vol 1. University Science Books, Sausalito
- Al-Ahmadi K, Al-Amri A, See L (2014) A spatial statistical analysis of the occurrence of earthquakes along the Red Sea floor spreading: clusters of seismicity. *Arab J Geosci* 7:2893–2904
- Ambraseys NN, Melville CP, Adams RD (1994) The seismicity of Egypt, Arabia and Red Sea. Cambridge University Press, Cambridge
- Andrews DJ (1986) Objective determination of source parameters and similarity of earthquakes of different size. *Earthq Source Mech* 37:259–267
- Badawy A (1999) Historical seismicity of Egypt. *Acta Geod Geophys Hung* 34(1–2):119–135
- Badreldin H, Abd el-aal AK, Toni M, El-Faragawy K (2019) Moment tensor inversion of small-to-moderate size local earthquakes in Egypt. *J Afr Earth Sci* 151(2019):153–172. <https://doi.org/10.1016/j.jafrearsci.2018.12.004>
- Bosworth W, Huchon P, McClay K (2005) The Red Sea and Gulf of Aden basins. *J Afr Earth Sci* 43:334–378
- Bosworth W, Montagna P, Pons-Branchu P, Rasul N, Taviani M (2017) Seismic hazards implications of uplifted Pleistocene coral terraces in the Gulf of Aqaba. *Sci Rep* 7:1–13
- Brune JN (1970) Tectonic stress and the spectra of seismic shear waves from earthquakes. *J Geophys Res* 75:4997–5009
- Cochran JR (2005) Northern Red Sea: nucleation of an oceanic spreading center within a continental rift. *Geochem Geophys Geosyst* 6:Q03006
- Coleman RG (1993) Geologic evolution of the Red Sea. Oxford monographs on geology and geophysics. Oxford University Press, Oxford, p 186
- Daggett P, Morgan P, Boulos FK, Hennin SF, El-Sherif AA, El-Sayed AA, Basta NZ, Melek YS (1986) Seismicity and active tectonics of the Egyptian Red Sea margin and the northern Red Sea. *Tectonophysics* 125:313–324
- Donner S, Rößler D, Krüger F, Ghods A, Strecker MR (2013) Segmented seismicity of the Mw 6.2 Baladeh earthquake sequence (Alborz Mountains, Iran) revealed from regional moment tensors. *J Seismol* 17(3):925–959
- El Gaby S, List FK, Tehrani R (1990) The basement complex of the Eastern Desert and Sinai. In: Said R (ed) The geology of Egypt. Balkema, Rotterdam, pp 175–184
- Eshelby JD (1957) The determination of the elastic field of an ellipsoidal inclusion, and related problems. *Proc R Soc Lond A Math Phys Eng Sci* 241(1226):376–396
- Ghebreab W (1998) Tectonics of the Red Sea region reassessed. *Earth Sci Rev* 45:144
- Havskov J, Ottemoller L (2010) Routine data processing in earthquake seismology: with sample data, exercises and software. Springer Science & Business Media
- Hempton M (1987) Constraints on Arabian plate motion and extensional history of the Red Sea. *Tectonics* 6:687–705

- Herrmann RB (2013) Computer programs in seismology: an evolving tool for instruction and research. *Seismol Res Lett* 84(6):1081–1088
- Herrmann RB, Wang CY (1985) A comparison of synthetic seismograms. *Bull Seismol Soc Am* 75(1):41–56
- Hosny A, El-Hady S, El-Ela AMA, Panza GF, Tealeb A, El Rahman MA (2009) Magma intrusion in the upper crust of the Abu Dabbab area, south east of Egypt from VP and VP=VS tomography. *Rendiconti Lincei* 20(1):1–19
- Hussein HM, Elenean KA, Marzouk IA, Korrat IM, El-Nader IA, Ghazala H, ElGabry MN (2013) Present-day tectonic stress regime in Egypt and surrounding area based on inversion of earthquake focal mechanisms. *J Afr Earth Sci* 81:1–15
- Iwata T, Irikura K (1988) Source parameters of the 1983 Japan Sea earthquake sequence. *J Phys Earth* 36(4):155–184
- Jost ML, Herrmann RB (1989) A student's guide to and review of moment tensor. *Seismol Res Lett* 60(2):37–57. <https://doi.org/10.1785/gssrl.60.2.37>
- Kanamori H (1994) Mechanics of earthquakes. *Annu Rev Earth Planet* 22:207–237
- Kebeasy RM (1990) Seismicity. The Geology of Egypt, Balkema, Rotterdam, pp 51–59
- Khalil SM, McClay KR (2001) Tectonic evolution of the northwestern Red Sea-Gulf of Suez rift system. In: Wilson RCL, Whitmarsh RB, Taylor B, Froitzheim N (eds) Non-volcanic rifting of continental margins: a comparison of evidence from land and sea, vol 187. Geological Society, London, pp 453–473. <https://doi.org/10.1144/GSL.SP.2001.187.01.22>
- Khalil SM, McClay KR (2002) Extensional fault-related folding, northwestern Red Sea, Egypt. *J Struct Geol* 24:743–762
- Khalil SM, McClay KR (2009) Structural control on syn-rift sedimentation, northwestern Red Sea margin, Egypt. *Mar Pet Geol* 26:1018–1034
- Khalil SM, McClay KR (2016) 3D geometry and kinematic evolution of extensional fault-related folds, NW Red Sea, Egypt. In: Childs C, Holdsworth RE, Jackson CA-L, Manzocchi T, Walsh JJ, Yielding G (eds) The geometry and growth of normal faults, vol 439. Geological Society, London, pp 109–130. <https://doi.org/10.1144/SP439.11>
- Klein FW (1978) Hypocenter location program HYPOINVERSE: part I. users guide to versions 1, 2, 3, and 4. Part II. Source listings and notes (No. 78–694). US Geological Survey
- Maamoun M, Allam A, Megahed A (1984) Seismicity of Egypt. *Bull Helwan Inst Astron Geophys* 4:109–160
- Mart Y, Horowitz A (1981) The tectonics of the Timna region in southern Israel and the evolution of the Dead Sea Rift. *Tectonophysics* 79:165–199
- Mart Y, Rabinowitz PD (1986) The northern Red Sea and the Dead Sea rift. *Tectonophysics* 124:85–113
- McClay KR, Nicols GJ, Khalil SM, Darwish M, Bosworth W (1998) Extensional tectonics and sedimentation, eastern Gulf of Suez, Egypt. In: Purser BH, Bosence DWJ (eds) Sedimentation and tectonics of Rift Basins: Red Sea-Gulf of Aden. Chapman and Hall, London, pp 223–238
- Meshref WM (1990) Tectonic framework. In: Said R (ed) The geology of Egypt. Balkema, Rotterdam, pp 113–155
- Mohamed EK, Hassoup A, Abou Elenean KM, Othman AA, Hamed DEM (2015) Earthquakes focal mechanism and stress field pattern in the northeastern part of Egypt. *NRIAG J Astron Geophys* 4(2):205–221
- Patton TL, Moustafa AR, Nelson RA, Abdine SA (1994) Tectonic evolution and structural setting of the Suez Rift. In: Landon SM (ed) Interior Rift Basins, vol 59. Memoirs, American Association of Petroleum Geologists, pp 7–55
- Saadalla H, Abd el-aal AK, Mohamed A, El-Faragawy K (2019) Determination of earthquake source parameters using the inversion of waveform data: a case of small earthquakes around High Dam Lake, Aswan region, Egypt. *J Afr Earth Sci* 151:403–416
- Saadalla H, Abd el-aal AK, Mohamed A, El-Faragawy K (2020) Characteristics of earthquakes recorded around the High Dam Lake with comparison to natural earthquakes using waveform inversion and source spectra. *Pure Appl Geophys*. <https://doi.org/10.1007/s00024-020-02490-4>
- Said R (1990) The geology of Egypt. Balkema, Rotterdam, p 734
- Saleh S, Jahr T, Jentzsch G, Saleh A, Abou Ashour NM (2006) Crustal evaluation of the Northern Red Sea rift and Gulf of Suez, Egypt from geophysical data: 3-dimensional modeling. *J Afr Earth Sci* 45:257–278
- Sawires R, Peláez JA, Fat-Helbary RE, Ibrahim HA (2016) An earthquake catalogue (2200 B.C. to 2013) for seismotectonic and seismic hazard assessment studies in Egypt. In: D'Amico S (ed) Earthquakes and their impact on society. Springer, Berlin, pp 97–136
- Stump BW, Johnson LR (1977) The determination of source properties by the linear inversion of seismograms. *Bull Seismol Soc Am* 67(6):1489–1502
- Zhang H, Eaton DW, Li G, Liu Y, Harrington RM (2016) Discriminating induced seismicity from natural earthquakes using moment tensors and source spectra. *J Geophys Res Solid Earth* 121(2):972–993
- Abou Elenean K (1997) Seismotectonic of Egypt in relation to the Mediterranean and Red Seas Tectonics. Ph.D. Thesis, Ain Shams Univ., Egypt
- Badawy A, Al-Gabry M, Girgis M (2010) Historical seismicity of Egypt, a study for previous catalogues producing revised weighted catalogue. In: The second Arab conference for astronomy and geophysics, 25–28 October 2010, Cairo, Egypt
- Bosworth W, McClay K (2001) Structural and stratigraphic evolution of the Gulf of Suez rift, Egypt: a synthesis. In: Ziegler PA, Cavazza W, Robertson AHF, Crasquin-Soleau S (eds) Peri-Tethys Memoir 6: Peri-Tethyan Rift/Wrench Basins and Passive Margins, Mémoires du Muséum National d'Histoire Naturelle de Paris, vol 186, pp 567–606
- Maamoun M (1979) Macro seismic observation of principal earthquakes in Egypt. *Bull Helwan Inst Astron Geophys*. 183
- Megahed A (2004) Seismic deformation studies on the northeastern part of Egypt. Ph.D. Thesis. Fac. of Sci., Geology Dept. Mansoura Univ.
- Riad S, Taeleb AA, El-Hadidy S, Basta NZ, Abou Elela AM, Mohamed AA, Khalil HA (2004) Ancient earthquakes from some Arabic sources and catalogue of Middle East historical earthquakes. EGSA, NARSS, UNDP, UNESCO, pp 71–91

Publisher's Note

Springer Nature remains neutral with regard to jurisdictional claims in published maps and institutional affiliations.

Submit your manuscript to a SpringerOpen[®] journal and benefit from:

- Convenient online submission
- Rigorous peer review
- Open access: articles freely available online
- High visibility within the field
- Retaining the copyright to your article

Submit your next manuscript at ► [springeropen.com](https://www.springeropen.com)